A POPULATION STUDY OF HOT JUPITER ATMOSPHERES

A. Tsiaras[1], I. P. Waldmann[1], T. Zingales[1,2], M. Rocchetto[1], G. Morello[1], M. Damiano[1,2], K. Karpouzas[3], G. Tinetti[1], L. K. McKemmish[1], J. Tennyson[1], S. N. Yurchenko[1]

[1]Department of Physics & Astronomy, University College London, Gower Street, WC1E6BT London, United Kingdom
[2]INAF–Osservatorio Astronomico di Palermo, Piazza del Parlamento 1, I-90134 Palermo, Italy and
[3]Department of Physics, Section of Astrophysics, Astronomy and Mechanics, Aristotle University of Thessaloniki, 541 24 Thessaloniki, Greece

Draft version April 19, 2017

ABSTRACT

We present here the analysis of 30 gaseous extrasolar planets, with temperatures between 600 and 2400 K and radii between 0.35 and 1.9 $R_{\rm Jup}$. The quality of the HST/WFC3 spatially-scanned data combined with our specialised analysis tools, allows us to create the largest and most self-consistent sample of exoplanetary transmission spectra to date and study the collective behaviour of warm and hot gaseous planets rather than isolated case-studies. We define a new metric, the Atmospheric Detectability Index (ADI) to evaluate the statistical significance of an atmospheric detection and find statistically significant atmospheres around 16 planets. For most of the Jupiters in our sample we find the detectability of their atmospheres to be dependent on the planetary radius but not on the planetary mass. This indicates that planetary gravity is a secondary factor in the evolution of planetary atmospheres. We detect the presence of water vapour in all the statistically detectable atmospheres and we cannot rule out its presence in the atmospheres of the others. In addition, TiO and/or VO signatures are detected with 4σ confidence in WASP-76 b, and they are most likely present on WASP-121 b. We find no correlation between expected signal-to-noise and atmospheric detectability for most targets. This has important implications for future large-scale surveys.

Keywords: methods: data analysis — methods: statistical — planets and satellites: atmospheres — techniques: spectroscopic

1. INTRODUCTION

We have progressed significantly from the first detections of atmospheric signatures in extrasolar planet atmospheres (e.g. Charbonneau et al. 2002; Richardson et al. 2007; Grillmair et al. 2008; Redfield et al. 2008; Swain et al. 2008; Tinetti et al. 2007; Knutson et al. 2008) and are rapidly entering the era of comparative exoplanetology. Whilst individual case-studies of hot-Jupiters (e.g. Konopacky et al. 2013; Macintosh et al. 2015; Brogi et al. 2013; Snellen et al. 2014; de Kok et al. 2013; Kreidberg et al. 2015; Stevenson et al. 2014; Tsiaras et al. 2016a; Todorov et al. 2013; Zellem et al. 2014; Line et al. 2016; Iyer et al. 2016; Deming et al. 2013; McCullough et al. 2014; Mandell et al. 2013) down to Neptune /Uranus (e.g. Fraine et al. 2014; Fukui et al. 2013; Ehrenreich et al. 2014; Knutson et al. 2014a; Stevenson et al. 2010; Morello et al. 2015) and super-Earth regimes (e.g. Bean et al. 2010; Berta et al. 2012; Tsiaras et al. 2016b; Demory et al. 2016; Knutson et al. 2014b; Kreidberg et al. 2014b) allow us to learn important new insights into the characteristics of exoplanets, we can only gain a limited insight into the global population and potential classifications of these foreign worlds. Population synthesis studies based on formation scenarios or statistics from the Kepler Space mission allow a first insight into the diversity of the exoplanet population (e.g. Lopez & Fortney 2014; Parmentier et al. 2016; Rogers 2015; Fortney et al. 2013). To break current model degeneracies, we need to observe the atmosphere of these objects.

With the maturation of data analysis techniques for the Hubble/WFC3 camera (and other ground-based instruments), we are rapidly entering the stage of atmospheric surveys. A notable study of 10 hot-Jupiters was presented last years (Sing et al. 2016) pointing out the need for more exoplanetary observations to reliably search for possible correlations in atmospheric parameters across this very diverse class of planets.

For such large-scale studies to fulfill their promise of comparative planetology, two criteria must be met: 1) Homogeneity in data analysis: spectra need to be uniformly analyzed to mitigate biases; 2) Quantitative and homogeneous atmospheric modeling: quantitative analysis using atmospheric retrieval software applied to all spectra allows the exact statistical comparability between planetary and atmospheric parameters.

Here we present the analysis of 30 hot-Jupiters observed with the HST/WFC3 camera, in the spatially scanning mode, ranging from warm-Neptunes to the very hot-Jupiters. Data were obtained from the publicly accessible pages of the NASA Mikulski Archive for Space Telescopes (MAST) archive. This presents the largest catalog of uniformly and quantitatively studied exoplanetary atmospheres to date, using the most precise observations currently available.

In the sections below, we present the data analysis and atmospheric retrieval frameworks used and discuss a new metric, the Atmospheric Detectability Index (ADI), for the quantitative assessment of atmospheric signature significances. As we will show in this work, atmospheric detectability is only weakly correlated with expected signal-to-noise ratio (S/N) given the orbital and the bulk parameters of the planets.

angelos.tsiaras.14@ucl.ac.uk

2. DATA ANALYSIS

We studied all the currently observed hot and gaseous planets with masses higher than $10\,\mathrm{M}_\oplus$ and estimated atmospheric features three times larger than the pre-calculated signal-to-noise ratio (pre-calculated (S/N > 3). The expected S/N was calculated assuming a mean molecular weight of 2.3 and using the expected flux provided by the WFC3 exposure time calculator. These are: GJ 436 b, GJ 3470, HAT-P-1 b, HAT-P-3 b, HAT-P-11 b, HAT-P-12 b, HAT-P-17 b, HAT-P-18 b, HAT-P-26 b, HAT-P-32 b, HAT-P-38 b, HAT-P-41 b, HD 149026 b, HD 189733 b, HD 209458 b, WASP-12 b, WASP-29 b, WASP-31 b, WASP-39 b, WASP-43 b, WASP-52 b, WASP-63 b, WASP-67 b, WASP-69 b, WASP-74 b, WASP-76 b, WASP-80 b, WASP-101 b, WASP-121 b, and XO-1 b. For some planets, other data sets using HST/STIS, Spitzer/IRAC and ground-based data exist (e.g. Danielski et al. 2014; Stevenson et al. 2014; Snellen et al. 2014; Line et al. 2016; Sing et al. 2016). Here we restrict ourselves to HST/WFC3 data for reasons of comparability and homogeneity in the analysis. We note also that in the absence of any overlap in the wavelength ranges probed by HST/STIS, HST/WFC3 and Spitzer/IRAC an absolute calibration at the level of 10 to 100 ppm between the different instruments cannot be achieved, making quantitative atmospheric retrievals sensitive to arbitrary offsets.

Despite being eligible, we did not include in our sample some of the available transit observations as they were affected by different kinds of systematics. These observations were: a) the second transit of HAT-P-11 b (ID: 12449, PI: D. Deming), due to the very large x-shifts of about 10 pixels, b) the first transit of HD 149026 b (ID: 14260, PI: D. Deming), as the spectrum was placed at the right edge of the detector, c) one transit of HAT-P-18 b (ID: 14099, PI: T. Evans), due to a possible star spot occultation, d) two transits of XO-2 b (ID: 13653, PI: C. Griffith), as the maximum flux per pixel exceeded the saturation level of 70,000 electrons, e) the third transit of GJ 3470 b (ID: 13665, PI: B. Benneke), in which the spectrum was possibly contaminated close to the $1.4\,\mu$m band.

From all the analyzed transit observations, the first HST orbit was removed because of the strong systematics that affect it. In some cases, a few spectroscopic images were also removed, as they were affected either by "snowballs" or by satellite trails. A complete list with the number of transit observations and HST orbits used, as well as the references for the parameters used, can be found in Table 1.

2.1. *Reduction and calibration*

Our analysis started from the raw spatially scanned spectroscopic images, using our specialized software for the analysis of WFC3 spatially scanned spectroscopic images (Tsiaras et al. 2016a,b). The reduction process included the following steps: zero-read subtraction, reference pixels correction, non-linearity correction, dark current subtraction, gain conversion, sky background subtraction, calibration, flat-field correction, and bad pixels/cosmic rays correction. In a broad sample like the current one, the possibility of observing additional sources in the field of view is high. Hence, we could not define the sky-area prior to the analysis, and the use of an automatic tool was necessary. The selected sky-area pixels were those with a flux level below a certain threshold – twice the flux mad (median absolute deviation) from the median flux – in all non-destructive reads. In cases where multiple transit observations were available (see Table 1), we calculated the position shifts by comparison with the first spectroscopic image of the first observation. This approach was followed to eliminate any systematic position shifts between the direct images of the different observations.

HD 189733 b — During the spatial scans of HD 189733 b the spectrum was shifted above the upper edge of the detector. Hence only the first three non-destructive reads were used from the forward scans and only the last five from the reverse scans. Due to the different exposure times, forward and reverse scans were processed independently as two different transit observations.

2.2. *Light-curves extraction*

Following the reduction process, we extracted the flux from the spatially scanned spectroscopic images to create the final transit light-curves per wavelength band. We considered one broad band (white) covering the whole wavelength range in which the G141 grism is sensitive ($1.088 - 1.68\,\mu$m), and two different sets of narrow bands (spectral). The resolving power of each set of narrow bands at $1.4\,\mu$m was 50 (low) and 70 (high), respectively. In both sets, the widths of the narrow bands were varying between 0.0188 and $0.0390\,\mu$m, in a way that the flux of a sun-like star would be equal in all the bands. The choice of the narrow bands sizes ensured an approximately uniform S/N across the planetary spectrum. In cases where additional sources existed in the field of view, we extracted our final light-curves from the differential non-destructive reads to avoid the overlap of different spectra during a scan (HAT-P-3 b, HAT-P-32 b, HAT-P-41 b, HD 189733 b, WASP-12 b, WASP-80 b, WASP-101 b, WASP-121 b). We also used this approach for the analysis of GJ 3470 b as the results for the white light-curve depths obtained from the two different transit observations were in a better agreement (1σ) compared to our common approach (2σ). Despite the absence of other stars in the field of view, this behavior indicates that there is small contamination from an additional source.

2.3. *Limb darkening coefficients*

We modeled the stellar limb darkening effect using the non-linear formula proposed by Claret (2000). The coefficients were fitted on the specific intensity profiles, evaluated at 100 angles, directly computed from the ATLAS model (Howarth 2011), for stars with effective temperatures higher than 4000 K, or PHOENIX (Allard et al. 2012) model, for stars with effective temperature lower than 4000 K, convoluted with the throughput of the G141 grism of the WFC3 camera. The stellar parameters used can be found in Table 2.

2.4. *White light-curves fitting*

As in previous observations with WFC3 (e.g. Kreidberg et al. 2015; Line et al. 2016; Evans et al. 2016; Wakeford et al. 2017) our extracted raw white light-curves

were affected by two kinds of time-dependent systematics, the long-term and short-term "ramp". The first is affecting each HST visit and has a linear behavior, while the second affects each orbit and has an exponential behavior. Additional systematics that cannot be described by the above functional forms are also very common (Wakeford et al. 2016). To account for these effects we fitted a model for the systematics simultaneously with the transit model (Kreidberg et al. 2014b; Tsiaras et al. 2016a). After an initial fit we scaled-up the uncertainties on the individual data points, in order for their median to match the standard deviation of the residuals, and fitted again. In this way we adopted more conservative values for the uncertainties of the fitted parameters, taking into account the systematics that were not described by our functional form. In addition, we let the parameters of the exponential short-term ramp vary between the first orbit and the rest of the orbits. This was necessary as in many cases the first orbit was affected in a different way compared to the other orbits. Finally, the parameters of the exponential short-term ramp also varied for the mid-orbit ramps caused by buffer dumps during an HST orbit.

All the white light-curves were fitted for the $R_{\rm p}/R_*$ and T_0 parameters, using fixed values for the P, e and ω parameters, as reported in the literature (see Table 2). Concerning the i and a/R_* parameters, the planets in our sample can be divided in three categories:

a) fitted for i and a/R_*: this category includes the white light-curves with observations during both the ingress and the egress (GJ 436 b, HAT-P-3 b, HAT-P-12 b, HAT-P-17 b and WASP-63 b, with all of them showing additional systematics).

b) successfully fitted with literature values for i and a/R_*: the majority of the white light-curves without observations during both the ingress and the egress is included in this category (GJ 3470 b, HAT-P-11 b, HAT-P-26 b, HAT-P-38 b, HAT-P-41 b, WASP-29 b, WASP-31 b, WASP-67 b, WASP-69 b, WASP-74 b, WASP-101 b).

c) other effects or additional systematics: the remaining white light-curves appeared to have additional signal and/or systematics in their residuals when the literature values for the i and a/R_* parameters were used. For HAT-P-1 b, HAT-P-18 b, WASP-39 b, and XO-1 b the residuals could be explained by slightly different values for the i and a/R_* parameters, while for HAT-P-32 b, HD 149026 b, HD 189733 b, HD 209548 b, WASP-12 b, WASP-43 b, WASP-52 b, WASP-80 b, WASP-76 b and WASP-121 b they could not. We note that the second group of planets orbit stars with temperatures either lower than 5000 K or higher that 6000 K. For the cooler stars a possible explanation is stellar activity, while for the hotter ones the discrepancy could be explained by the difference between more realistic, 3-D, stellar models and the 1-D models used for the calculation of the limb darkening coefficients (Hayek et al. 2012). Unfortunately, the absence of any information on the duration of the transit did not allow us to constrain whether the remaining residuals were due to stellar activity, limb darkening coefficients or additional instrumental systematics.

2.5. *Spectral light-curves fitting*

Finally, we fitted the spectral light-curves using the divide-white method introduced by Kreidberg et al.

(2014b), where the white light-curve was used as a comparison source, with the addition of a normalization factor and a wavelength-dependent slope, linear with time6. In the same way as for the white light-curves, we performed an initial fit and then scaled-up the uncertainties on the individual data points based on the standard deviation of the residuals, and fitted again. Concerning the fitting of the spectral light-curves, the wavelength-dependent slope was not correlated with the $R_{\rm p}/R_*$ parameter, despite the strength of the slope. The only exception was HAT-P-17 b, as no observations after the transit were included in this data set. However, the strength of the slope was insignificant throughout the spectrum of HAT-P-17 b ($<1\sigma$). For each planet, two final spectra were extracted at different resolutions (high and low, from the two sets of narrow bands). For the cases were multiple transit observations were available, the final spectra were the weighted average of the individual spectra, corrected for potential offsets in the white light-curve depth from one transit to another.

WASP-80 b — From the spectrum of WASP-80 b, one data point at $1.4\,\mu$m was excluded as it was contaminated by the zeroth order of the spectrum of a nearby source.

WASP-12 b — The spectrum of WASP-12 b was contaminated by a very close companion. To correct for this effect, we used the starring-mode spectroscopic images included in the data set. From those images, we calculated a dilution factor, which we then used to correct the spectra (Kreidberg et al. 2015).

WASP-43 b — In our final sample, a number of spectra shows a decreasing trend towards longer wavelengths. For temperatures higher than 4700 K, the sample includes planets with high impact parameters which do not show this trend. This result indicates that the trends are not caused by uncertainties in the limb darkening coefficients as, in this case, all the planets with high impact would be affected. WASP-43 b is the only planet below 4700 K with high impact parameters that was affected by a trend, decreasing with wavelength. To test the effect of limb darkening for this planet, we fitted for a linear limb darkening coefficient, alongside with the other parameters. We found the trend in the spectrum to be less strong and in agreement with the literature (Kreidberg et al. 2014a). The final spectrum of WASP-43 b reported includes the limb darkening fitting.

3. ATMOSPHERIC MODELING

The observed spectra were fitted using the Bayesian atmospheric retrieval framework $\mathcal{T}$-REx (Waldmann et al. 2015b,a). $\mathcal{T}$-REx fully maps the atmospheric correlated parameters retrieved from the observed spectra through the use of nested sampling (Skilling 2006; Feroz et al. 2009). We modeled the transmission spectra using a variety of possible molecular opacities, namely H_2O, CH_4, CO, CO_2, NH_3, TiO and VO. For the vast majority of cases, water is the only detectable signal together with clouds/hazes. However, TiO and VO were detected in WASP-76 b and WASP-121 b. Below, we briefly describe the priors adopted, the general atmospheric parameterizations, opacity sources and cloud parameterization. All

input parameters and full model outputs for each planet can be found in the accompanying data pack.

3.1. General setup

The atmospheres of the planets analyzed here were simulated to range from 10 to 10^7 Pa and sampled uniformly in log-space by 50 atmospheric layers. We tested for potential under-sampling of the atmosphere by running test retrievals at 250 and 50 layers. No significant degradation of retrieval accuracy for HST/WFC3 data could be found. Each trace-gas opacity was allowed to vary from 10^{-8} to 10^{-1} mixing ratios, as a log-uniform prior. From here forth all priors are assumed to be uniform unless specified otherwise. We calculated planetary equilibrium temperatures assuming geometric albedos varying from 0.6 to zero and emissivity from 0.5 to 1 to calculate the temperature prior range. An isothermal temperature-pressure profile was assumed. While this is an oversimplification and can lead to retrieval biases (Rocchetto et al. 2016), the restrictive wavelength ranges of 1.1 to $1.8\,\mu$m do not allow differentiation of an isothermal from a more complex profile. We adopted the planetary radius uncertainties reported in the literature as prior bounds and corrected them if needed.

3.2. Opacity sources

Initially, exploratory retrievals were run to include a wide range of molecular opacities: H_2O, HCN, NH_3, CH_4, CO_2, CO, NO, SiO, TiO, VO, H_2S, and C_2H_2. No significant contributions were found but for H_2O, TiO and VO. We hence restricted further retrievals to a smaller set of molecules: H_2O (Barber et al. 2006), CO (Rothman et al. 2010), CO_2 (Rothman et al. 2010), CH_4 (Yurchenko & Tennyson 2014) and NH_3 (Yurchenko et al. 2011). VO (McKemmish et al. 2016) and TiO (McKemmish in prep.) were added to the mix for planets with equilibrium temperatures exceeding 1400 K. Tau-REx is designed to operate with either absorption cross-sections or correlated-k coefficients. Both cross-sections and k-tables were computed from very high-resolution $(R > 10^6)$ cross-sections, which in turn were calculated from molecular line lists obtained from ExoMol (Tennyson et al. 2016), HITEMP (Rothman et al. 2010) and HITRAN (Rothman et al. 2013). Temperature and pressure dependent line-broadening was included, taking into account J-dependence where available (Pine 1992). The absorption cross-sections were then binned to a constant resolution of R = 7000 and the transmission forward models were calculated at this resolution before binning to the resolution of the data. Given the resolutions, wavelength range and uncertainties of the data at hand, we find no differences between the use of cross-section and k-tables in the final retrieval results. Rayleigh scattering and collision induced absorption of H_2-H_2 and H_2-He was also included (Borysow et al. 2001; Borysow 2002).

3.3. Cloud parameterization

A variety of cloud parameterizations of varying complexity exist in the context of atmospheric retrieval studies (e.g. Benneke & Seager 2012; Line et al. 2016; Barstow et al. 2013; Griffith 2014). Here we adopted the parameterization of Lee et al. (2013), which also finds implementation in an atmospheric retrieval context in Lavie et al.

(2016). In transmission spectroscopy, the cloud optical depth as function of wavelength, $\tau_{c1,\lambda}$, is given by:

$$\tau_{c1,\lambda} = \int_0^{l(z)} Q_{ext,\lambda}\pi\alpha^2\chi_c(z')\rho_N(z')dl \qquad (1)$$

where z is the height in the atmosphere, α is the particle size of the cloud/haze, dl is the path length through the atmosphere, χ_c is the cloud mixing-ratio, ρ_N is the atmospheric number density, and $Q_{ext,\lambda}$ is the cloud extinction coefficient given by:

$$Q_{ext,\lambda} = \frac{5}{Q_0 x^{-4} + x^{0.2}} \qquad (2)$$

where $x = 2\pi\alpha/\lambda$ and Q_0 determines the peak of $Q_{ext,\lambda}$. This can be understood as a cloud compositional parameter (Lee et al. 2013). For $x \ll \lambda$, the formalism reduces to pure Rayleigh scattering. In addition to the above, we implemented an optically thick grey-cloud cover, parameterized as follows:

$$\tau_{c2} = \begin{cases} 1, & \text{if } P < P_{\text{cloud-top}} \\ 0, & \text{otherwise} \end{cases} \qquad (3)$$

where $P_{\text{cloud-top}}$ is the cloud-top pressure. This dual parameterization allowed us to model optically thick cloud decks with a semi-transparent, hazy, atmosphere above $P_{\text{cloud-top}}$.

We initially kept Q_0, χ_c, α, and $P_{\text{cloud-top}}$ as free cloud parameters but found HST/WFC3 data to be insufficient to constrain Q_0. We set a log-uniform prior of χ_c ranging from 10^{-40} to 10^{-10}, particle size from 10^{-5} to $10\,\mu$m, compositional prior from 1 to 100 and cloud top-pressure from 10 to 10^7 Pa (Lee et al. 2013).

3.4. Free parameters and model selection

In the end, we had nine free parameters: four molecular abundances, temperature, planet radius and three cloud-deck parameters. Each one of the two spectra per planet at different resolutions was retrieved, yielding 60 retrievals in total. However, we found no difference between the information retrieved from the two spectra at different resolution.

3.5. Atmospheric Detection Index (ADI)

In order to quantify the detection significance of an atmosphere, we devised the Atmospheric Detection Index (ADI). The ADI is the positively defined Bayes Factor between the nominal atmospheric model (M_N) and a flat-line model (M_F). As stated above, the nominal model contains molecular opacities, cloud/haze opacities $(\tau_{c1,\lambda}, \tau_{c2})$ collision induced absorption of H_2-H_2/H_2-He and Rayleigh scattering. Other free parameters are the planet radius, R_p, and the temperature of the isothermal TP-profile, T_{iso}. The flat-line model contains only grey-cloud opacities, τ_{c2}, R_p and T_{iso}. This parameterization always results in a flat-line spectrum but includes the model degeneracies found between cloud top-pressure, planet-radius and temperature. This way we capture both cloudy as well as clear sky scenarios. As the ADI is a fully Bayesian model selection metric, we naturally impose Occam's razor to our atmosphere detection significance.

We obtained the Bayesian evidence of our nominal model, E_N, and of the pure-cloud/no-atmosphere model, E_F, and calculated the ADI as follows:

$$ADI = \begin{cases} \log(E_N) - \log(E_F), & \text{if } \log(E_N) > \log(E_F) \\ 0, & \text{otherwise} \end{cases}$$

(4)

The ADI is a positively defined metric and equivalent to the logarithmic Bayes Factor (Kass & Raftery 1995) where $\log(E_N) > \log(E_F)$. From the two types of spectra for each planet, we selected the one with the higher ADI.

4. RESULTS AND DISCUSSION

4.1. *Atmospheric detectability*

The higher-resolution spectra obtained for all the planets in our sample are presented in Table 3. We note that the ADI intrinsically features a dependence on spectral resolution and photon noise. We hence calculated the ADI for both, high and low resolution spectra extracted per planet and selected the spectral resolution corresponding to the higher ADI. Though we note that no substantial differences were found. The ADI index has been reported for all the planets in Figure 1 and Table 4. The spectra in Figure 1 are ordered by decreasing ADI.

Given the definition of the ADI index in the previous section, an atmosphere is detected at 3σ and 5σ level for ADIs above 3 and 11 respectively. In our sample we find that 16 out of 30 planets feature statistically significant atmospheres, with ADIs higher than 3. While parameter constraints of atmospheric models for many of the planets with ADIs lower than 3 can be significant, indicating the presence of water (WASP-80 b, WASP-43 b, HAT-P-12 b, HAT-P-38 b, WASP-31 b, WASP-63 b, GJ 3470 b, WASP-67 b, WASP-74 b), the model as a whole is not. Hence, ADIs below 3 signify atmospheric non-detections, as the spectral feature amplitudes are insufficient (given the uncertainties in the data) to favor the more complex atmospheric model, M_N over the lower dimensional flat-line model M_F. To verify the presence of water in these planets, additional observations are necessary. We have to note here that for WASP-43 b the presence of water has been confirmed using additional observations during the eclipse of the planet (Kreidberg et al. 2014a). By adopting the ADI, we were able to draw several important conclusions about this population of exoplanets and spectroscopic observations of exoplanets in general.

Previous population studies suggested that the observed spectra do not show the expected modulations, given the physical characteristics of the planets (Iyer et al. 2016; Sing et al. 2016). Interestingly, even in this larger sample with all the planets expected to feature some modulations given the precision of the observations, the ADI does not correlate with the pre-calculated S/N. To exclude any observational biases we repeated the S/N calculation using the median uncertainty of our final observed high-resolution spectra instead of the pre-calculated uncertainties, we will refer to this quantity as observationally-corrected S/N (o.c. S/N). Interestingly, we find that for the planets with an o.c. S/N below 15, the ADI index is not correlated to the o.c. S/N (Figure 2). In this regime we can find planets that scored highly on paper in terms of potential detections of atmo-

spheric features but turned out to be difficult to interpret (e.g. WASP-101 b), and planets that appeared relatively challenging to observe on paper but delivered very solid detections (e.g. XO-1 b). This absence of predictability showcases the need for exploratory observations prior to major time investments with large-scale facilities such as the JWST.

Considering the warm and hot Jupiters in our sample ($M > 0.16\,M_{Jup}$), there are two groups: a) a outlying group of five planets with large radii but not detectable atmospheres (WASP-31 b, WASP-63 b, WASP-67 b, WASP-74 b and WASP-101 b) which covers a wide range of planetary radii and shows no correlation with stellar or orbital parameters and b) all the remaining Jupiters for which the Pearson correlation coefficient indicates that the ADI is more strongly correlated with the planetary radius (0.68, p-value=0.05%) than the planetary temperature (0.47, p-value=3%) or surface gravity (-0.47, p-value=3%) but not correlated with the planetary mass (0.2, p-value=37%). These results indicate that planetary surface gravity is a secondary factor in identifying inflated atmospheres (Laughlin et al. 2011; Weiss et al. 2013; Spiegel & Burrows 2013).

Very hot and highly irradiated planets, with atmospheric temperatures above 1800 K feature high ADI atmospheres. Our quantitative retrievals suggest that the cloud top-pressures in these planets are significantly high, meaning clouds are deep in the atmosphere, if present at all (Table 4), while retrieved water abundances are constant within the errors. Whilst we cannot determine the absolute atmospheric water abundances, given the relative narrow wavelength range probed, we can exclude scenarios where water is significantly destroyed or depleted in the upper atmospheres of irradiated and inflated hot-Jupiters. In addition, the spectra of HAT-P-41 b, WASP-12 b and WASP-121 b show no contribution from photochemical hazes (Zahnle et al. 2009; Kopparapu et al. 2012; Miller-Ricci Kempton et al. 2012). We can conclude that planets with temperatures higher than 1800 K feature clear atmospheres, confirming that most of the element-carriers are present in a gaseous form at such hot temperatures.

4.2. *Molecular opacities detected*

The 16 spectra which show statistically significant atmospheres presented here are well described with a combination of grey-clouds, extended, particulate Rayleigh curves and water. Two notable exceptions are WASP-76 b (see Figures 4 and 5) and WASP-121 b. Both planets are hot Jupiters with equilibrium temperatures of $\sim$2000 K. The retrieval results show that the atmosphere is haze free (i.e. clear) and TiO, VO and H_2O opacities determine the observed spectral shape. TiO/VO is detected with a Bayes Factor of 6.55 (4.0σ significance) when compared to a pure-water and haze dominated atmosphere for WASP-76 b, while the two cases are not statistically distinguishable for WASP-121 b. The sparse sampling of HST/WFC3 data and the short wavelength ranges do not allow us to conclusively exclude atmospheric haze models for these planets at this stage, though we note that the particulate extended Rayleigh curve would be unusually strong. Observations at longer wavelength ranges are required to conclude.

The remaining 14 spectra without a statistically sig-

nificant atmosphere can be explained by either opaque, high-altitude, clouds or low water abundances, as no-atmosphere models are unlikely for gas-giant planets. Given the uncertainties in the observed spectra, we are sensitive to water mixing ratio higher than 10^{-8}, for cloud-free atmospheres. We also note that combinations of water depletion and high-altitude clouds cannot be ruled out. Current space and ground-based data cannot constrain absolute abundances of trace gases beyond their detection. Future instrumentation such as the JWST or dedicated space missions probing a broader wavelength range will be able to break these degeneracies.

The spectra of 11 out of the 30 planets in our sample have been previously studied. Concerning the detection of an atmosphere and the presence of water vapor our results are in agreement with the literature. These planets are: GJ 436 b (Knutson et al. 2014a), HAT-P-1 b (Wakeford et al. 2013), HAT-P-11 b (Fraine et al. 2014), HD 209458 b (Deming et al. 2013), HD 189733 b (McCullough et al. 2014), WASP-12 b (Kreidberg et al. 2015), WASP-31 b (Sing et al. 2015), WASP-43 b (Kreidberg et al. 2014a), WASP-101 b (Wakeford et al. 2017), WASP-121 b (Evans et al. 2016) and XO-1 b (Deming et al. 2013).

5. CONCLUSIONS

We have presented here the largest catalog of exoplanet atmospheres and atmospheric retrievals to date. Using the most precise data available, analyzed by our specialized tool for WFC3 spatially scanned observations, combined with our fully Bayesian spectral retrieval code and the most accurate molecular line lists, we are able to provide the first fully self-consistent, stable and statistically evaluated reference catalog for comparative exoplanetary characterization.

All software used to create this catalog, and all the intermediate and final data products will be publicly available to the community, allowing for reproducibility of the results and further analysis.

Currently, the extracted light-curves and spectra, the fitting data and results, and additional plots for each data set and each planet are available at http://bit.ly/HSTDATA [*Please note, this link is a temporary dropbox. We intend to move the data to a permanent open-access portal soon*].

We defined a new metric to estimate the significance of an atmospheric observation, the Atmospheric Detection Index (ADI). The ADI is the positively-defined logarithmic Bayes Factor between the best-fit water-only model and a grey-cloud/no-atmosphere family of models. It is markedly different to a more classical straight-line rejection as it compares detectable atmospheric features to the full range of possible non-detection models given the data. Amongst the wide diversity of planets, we find about half to have strongly detectable atmospheres featuring water signatures (ADI > 3). We cannot rule out the existence of clouds or water depletion in the remaining, not statistically significant, atmospheres (ADI < 3). Warm and hot Jupiters, with the exception of a distinct group of five hot Jupiters that likely feature very high al-

titude clouds, follow a clear trend between the ADI and the planetary radius. We find that simple S/N predictions are insufficient for target selection requiring comprehensive spectroscopic observations of targets prior to more detailed studies using large scale observation programs. Population studies such as this one are fundamental in understanding the complex nature and evolutionary history of planets.

REFERENCES

Allard, F., Homeier, D., & Freytag, B. 2012, Philosophical Transactions of the Royal Society of London Series A, 370, 2765

Anderson, D. R., Collier Cameron, A., Hellier, C., et al. 2011, A&A, 531, A60

Anderson, D. R., Collier Cameron, A., Delrez, L., et al. 2014, MNRAS, 445, 1114

Bakos, G. Á., Noyes, R. W., Kovács, G., et al. 2007, ApJ, 656, 552

Bakos, G. Á., Torres, G., Pál, A., et al. 2010, ApJ, 710, 1724

Barber, R. J., Tennyson, J., Harris, G. J., & Tolchenov, R. N. 2006, MNRAS, 368, 1087

Barstow, J. K., Aigrain, S., Irwin, P. G. J., Fletcher, L. N., & Lee, J.-M. 2013, MNRAS, 434, 2616

Bean, J. L., Miller-Ricci Kempton, E., & Homeier, D. 2010, Nature, 468, 669

Benneke, B., & Seager, S. 2012, ApJ, 753, 100

Berta, Z. K., Charbonneau, D., Desert, J.-M., et al. 2012, Nature, 747, 35

Biddle, L. I., Pearson, K. A., Crossfield, I. J. M., et al. 2014, MNRAS, 443, 1810

Borysow, A. 2002, A&A, 390, 779

Borysow, A., Jorgensen, U. G., & Fu, Y. 2001, J. Quant. Spec. Radiat. Transf., 68, 235

Brogi, M., Snellen, I. A. G., de Kok, R. J., et al. 2013, ApJ, 767, 27

Charbonneau, D., Brown, T. M., Noyes, R. W., & Gilliland, R. L. 2002, APJ, 568, 377

Claret, A. 2000, A&A, 363, 1081

Collins, K. A., Kielkopf, J. F., & Stassun, K. G. 2017, AJ, 153, 78

Danielski, C., Deroo, P., Waldmann, I. P., et al. 2014, ApJ, 785, 35

de Kok, R. J., Brogi, M., Snellen, I. A. G., et al. 2013, A&A, 554, A82

Delrez, L., Santerne, A., Almenara, J.-M., et al. 2016, MNRAS, 458, 4025

Deming, D., Wilkins, A., McCullough, P., et al. 2013, ApJ, 774, 95

Demory, B.-O., Gillon, M., de Wit, J., et al. 2016, Nature, 532, 207

Ehrenreich, D., Bonfils, X., Lovis, C., et al. 2014, A&A, 570, A89

Esposito, M., Covino, E., Mancini, L., et al. 2014, A&A, 564, L13

Evans, T. M., Sing, D. K., Wakeford, H. R., et al. 2016, ApJL, 822, L4

Faedi, F., Barros, S. C. C., Anderson, D. R., et al. 2011, A&A, 531, A40

Feroz, F., Hobson, M. P., & Bridges, M. 2009, MNRAS, 398, 1601

Fortney, J. J., Mordasini, C., Nettelmann, N., et al. 2013, ApJ, 775, 80

Fraine, J., Deming, D., Benneke, B., et al. 2014, Nature, 513, 526

Fukui, A., Narita, N., Kurosaki, K., et al. 2013, ApJ, 770, 95

Griffith, C. A. 2014, Philosophical Transactions of the Royal Society of London Series A, 372, 20130086

Grillmair, C. J., Burrows, A., Charbonneau, D., et al. 2008, Nature, 456, 767

Hartman, J. D., Bakos, G. Á., Torres, G., et al. 2009, ApJ, 706, 785

Hartman, J. D., Bakos, G. Á., Kipping, D. M., et al. 2011a, ApJ, 728, 138

Hartman, J. D., Bakos, G. Á., Torres, G., et al. 2011b, ApJ, 742, 59

Hartman, J. D., Bakos, G. Á., Béky, B., et al. 2012, AJ, 144, 139

Hayek, W., Sing, D., Pont, F., & Asplund, M. 2012, A&A, 539, A102

Hébrard, G., Collier Cameron, A., Brown, D. J. A., et al. 2013, A&A, 549, A134

Hellier, C., Anderson, D. R., Collier Cameron, A., et al. 2010, ApJL, 723, L60

—. 2011, A&A, 535, L7

—. 2012, MNRAS, 426, 739

Hellier, C., Anderson, D. R., Cameron, A. C., et al. 2014, MNRAS, 440, 1982

Hellier, C., Anderson, D. R., Collier Cameron, A., et al. 2015, AJ, 150, 18

Howard, A. W., Bakos, G. Á., Hartman, J., et al. 2012, ApJ, 749, 134

Howarth, I. D. 2011, MNRAS, 413, 1515

Iyer, A. R., Swain, M., Zellem, R. T., et al. 2016, ApJ, 823, 109

Kass, E. R., & Raftery, E. A. 1995, Journal of the American Statistical Association, 90, 773

Knutson, H. A., Benneke, B., Deming, D., & Homeier, D. 2014a, Nature, 505, 66

Knutson, H. A., Charbonneau, D., Allen, L. E., Burrows, A., & Megeath, S. T. 2008, ApJ, 673, 526

Knutson, H. A., Dragomir, D., Kreidberg, L., et al. 2014b, ApJ, 794, 155

Konopacky, Q. M., Barman, T. S., Macintosh, B. A., & Marois, C. 2013, Science, 339, 1398

Kopparapu, R. k., Kasting, J. F., & Zahnle, K. J. 2012, ApJ, 745, 77

Kreidberg, L., Bean, J. L., Désert, J.-M., et al. 2014a, ApJL, 793, L27

—. 2014b, Nature, 505, 69

Kreidberg, L., Line, M. R., Bean, J. L., et al. 2015, ApJ, 814, 66

Lanotte, A. A., Gillon, M., Demory, B.-O., et al. 2014, A&A, 572, A73

Laughlin, G., Crismani, M., & Adams, F. C. 2011, ApJL, 729, L7

Lavie, B., Mendonça, J. M., Mordasini, C., et al. 2016, ArXiv e-prints, arXiv:1610.03216

Lee, J.-M., Heng, K., & Irwin, P. G. J. 2013, ApJ, 778, 97

Line, M. R., Stevenson, K. B., Bean, J., et al. 2016, AJ, 152, 203

Lopez, E. D., & Fortney, J. J. 2014, ApJ, 792, 1

Macintosh, B. A., Graham, J. R., Barman, T. S., et al. 2015, Science, 350, 64

Mandell, A. M., Mandell, A. M., Haynes, K., et al. 2013, ApJ, 779, 128

McCullough, P. R., Crouzet, N., Deming, D., & Madhusudhan, N. 2014, ApJ, 791, 55

McKemmish, L. K., Yurchenko, S. N., & Tennyson, J. 2016, MNRAS, 463, 771

Miller-Ricci Kempton, E., Zahnle, K., & Fortney, J. J. 2012, ApJ, 745, 3

Morello, G., Waldmann, I. P., Tinetti, G., et al. 2015, ApJ, 802, 117

Parmentier, V., Fortney, J. J., Showman, A. P., Morley, C., & Marley, M. S. 2016, ApJ, 828, 22

Pine, A. S. 1992, J. Chem. Phys., 97, 773

Redfield, S., Endl, M., Cochran, W. D., & Koesterke, L. 2008, ApJl, 673, L87

Richardson, L. J., Deming, D., Horning, K., Seager, S., & Harrington, J. 2007, Nature, 445, 892

Rocchetto, M., Waldmann, I. P., Venot, O., Lagage, P.-O., & Tinetti, G. 2016, ApJ, 833, 120

Rogers, L. A. 2015, ApJ, 801, 41

Rothman, L. S., Gordon, I. E., Barber, R. J., et al. 2010, J. Quant. Spec. Radiat. Transf., 111, 2139

Rothman, L. S., Gordon, I. E., Babikov, Y., et al. 2013, J. Quant. Spec. Radiat. Transf., 130, 4

Sato, B., Hartman, J. D., Bakos, G. Á., et al. 2012, PASJ, 64, 97

Sing, D. K., Wakeford, H. R., Showman, A. P., et al. 2015, MNRAS, 446, 2428

Sing, D. K., Fortney, J. J., Nikolov, N., et al. 2016, Nature, 529, 59

Skilling, J. 2006, Bayesian Analysis, 1, 833

Snellen, I. A. G., Brandl, B. R., de Kok, R. J., et al. 2014, Nature, 509, 63

Spiegel, D. S., & Burrows, A. 2013, ApJ, 772, 76

Stevenson, K. B., Bean, J. L., Seifahrt, A., et al. 2014, AJ, 147, 161

Stevenson, K. B., Harrington, J., Nymeyer, S., et al. 2010, Nature, 464, 1161

Stevenson, K. B., Desert, J.-M., Line, M. R., et al. 2014, Science, 346, 838

Swain, M. R., Vasisht, G., & Tinetti, G. 2008, Nature, 452, 329

Tennyson, J., Yurchenko, S. N., Al-Refaie, A. F., et al. 2016, Journal of Molecular Spectroscopy, 327, 73

Tinetti, G., Vidal-Madjar, A., Liang, M.-C., et al. 2007, Nature, 448, 169

Todorov, K. O., Deming, D., Knutson, H. A., et al. 2013, ApJ, 770, 102

Torres, G., Winn, J. N., & Holman, M. J. 2008, ApJ, 677, 1324

Triaud, A. H. M. J., Gillon, M., Ehrenreich, D., et al. 2015, MNRAS, 450, 2279

Tsiaras, A., Waldmann, I. P., Rocchetto, M., et al. 2016a, ApJ, 832, 202

Tsiaras, A., Rocchetto, M., Waldmann, I. P., et al. 2016b, ApJ, 820, 99

Wakeford, H. R., Sing, D. K., Evans, T., Deming, D., & Mandell, A. 2016, ApJ, 819, 10

Wakeford, H. R., Sing, D. K., Deming, D., et al. 2013, MNRAS, 435, 3481

Wakeford, H. R., Stevenson, K. B., Lewis, N. K., et al. 2017, ApJL, 835, L12

Waldmann, I. P., Rocchetto, M., Tinetti, G., et al. 2015a, ApJ, 813, 13

Waldmann, I. P., Tinetti, G., Rocchetto, M., et al. 2015b, ApJ, 802, 107

Weiss, L. M., Marcy, G. W., Rowe, J. F., et al. 2013, ApJ, 768, 14

West, R. G., Hellier, C., Almenara, J.-M., et al. 2016, A&A, 585, A126

Yurchenko, S. N., Barber, R. J., & Tennyson, J. 2011, MNRAS, 413, 1828

Yurchenko, S. N., & Tennyson, J. 2014, MNRAS, 440, 1649

Zahnle, K., Marley, M. S., Freedman, R. S., Lodders, K., & Fortney, J. J. 2009, ApJL, 701, L20

Zellem, R. T., Griffith, C. A., Deroo, P., Swain, M., & Waldmann, I. 2014, ApJ, 796, 48
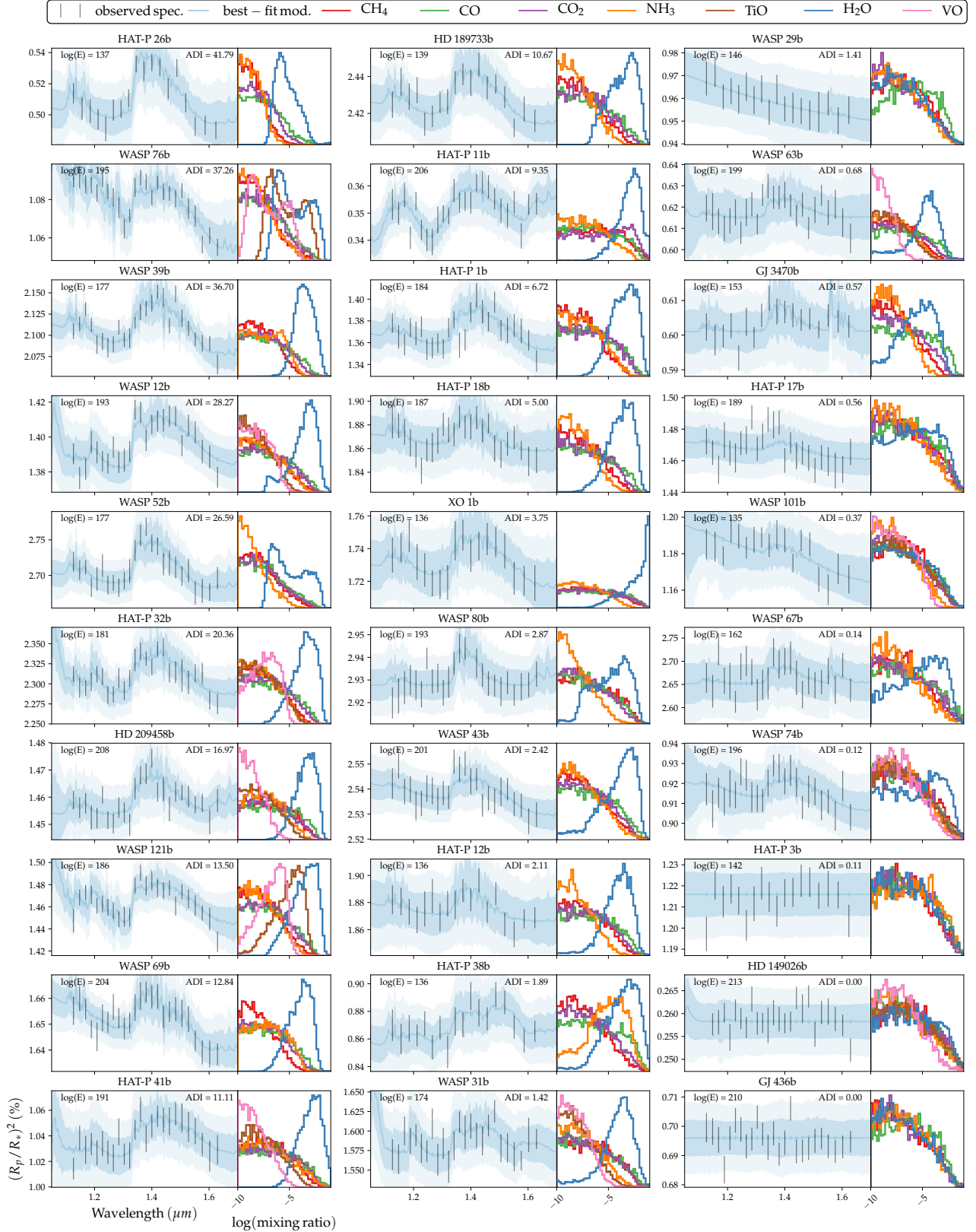
Figure 1. Atmospheric modeling results for all 30 planets in the sample. The planets are ordered based on the ADI index. The Bayesian evidence, log(E), of the best-fit model for each planet is also reported. Each panel shows, at left, the spectrum and the best-fit model and, at right, the posterior distributions of the abundances of the different molecules fitted.
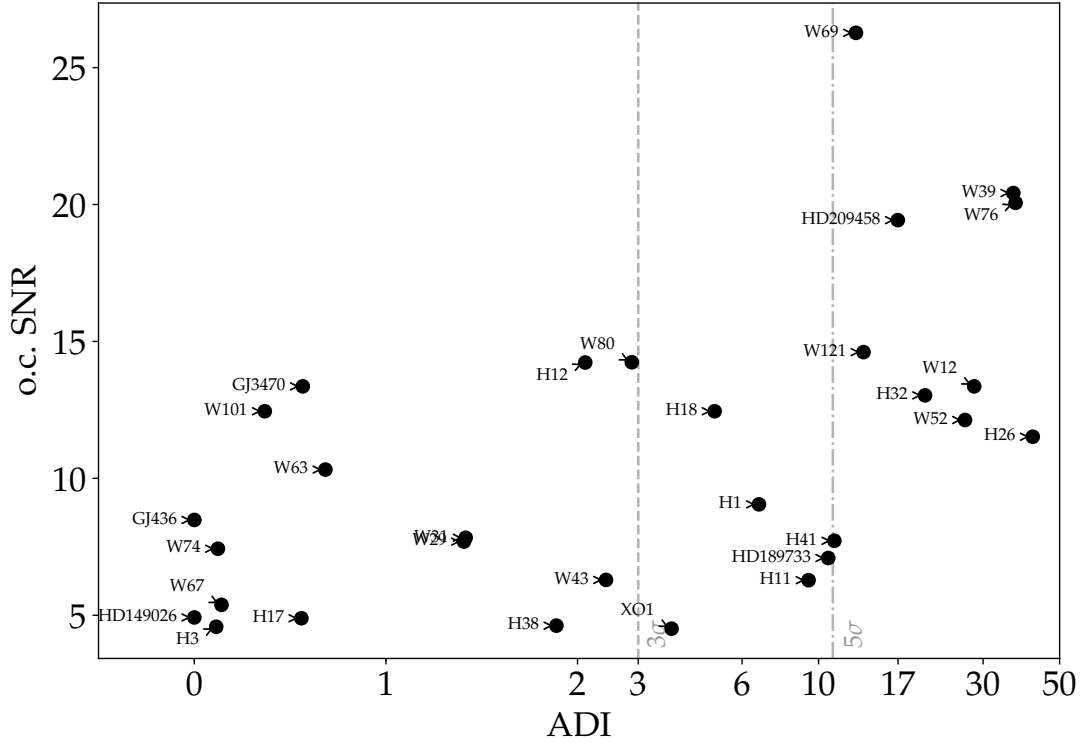
Figure 2. The o.c. S/N as a function of the ADI shows that planets with o.c. S/N > 15 are always detectable but no correlation between ADI and o.c. S/N can be found for planets with o.c S/N < 15.
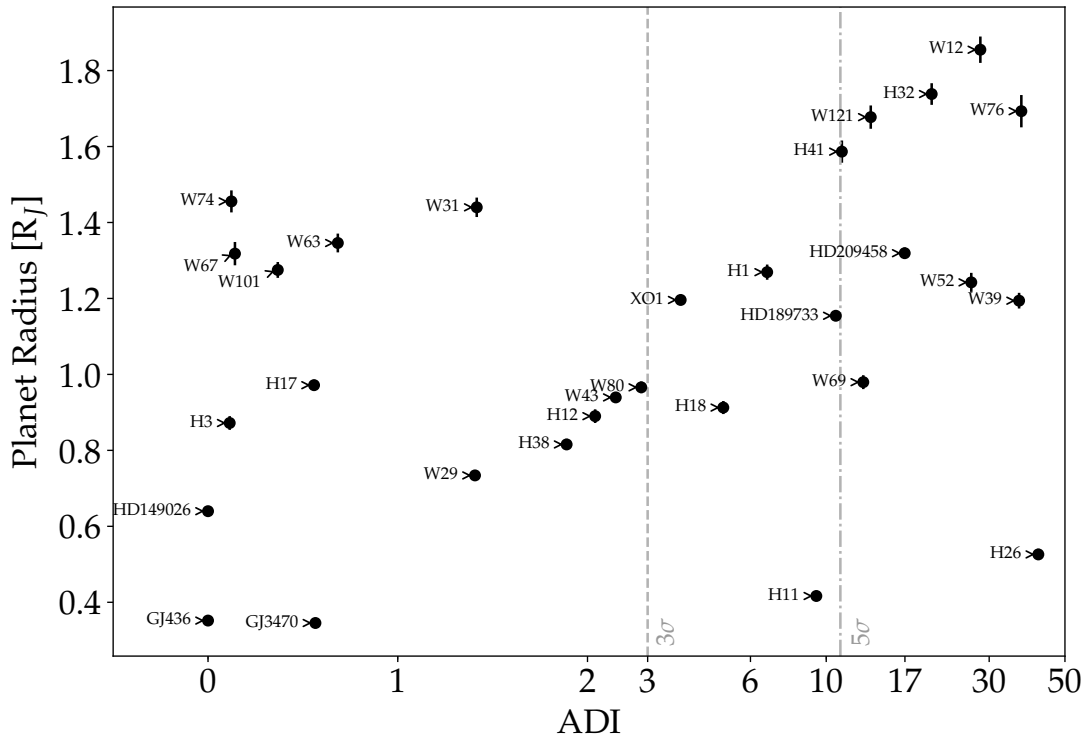
Figure 3. A positive correlation exists between the planet radius and ADI, with larger planets generally featuring more detectable atmospheres. However, We note an outlying cluster of five planets, including WASP-31 b, WASP-63 b, WASP-67 b, WASP-74 b and WASP-101 b. These low ADIs may indicate high-altitude cloud covers, or water depleted atmospheres.
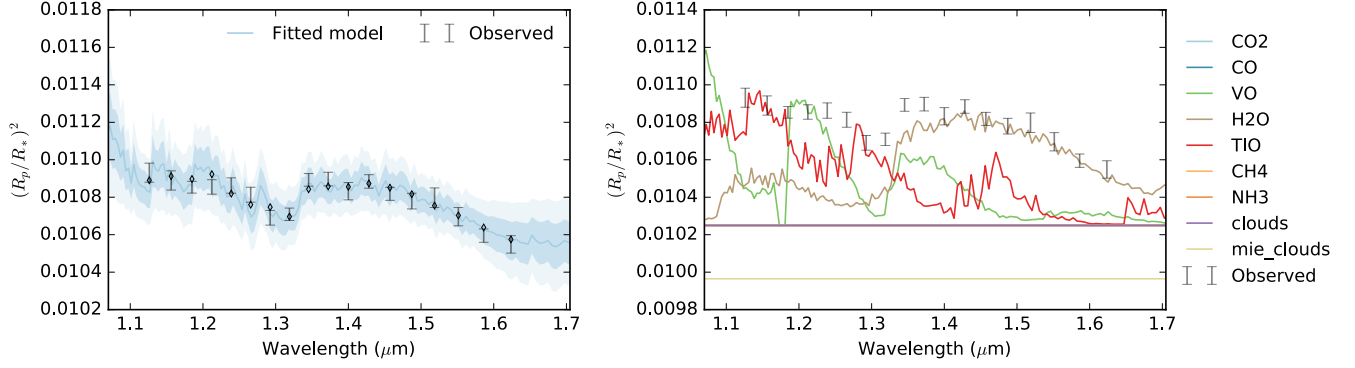
Figure 4. Left: Best fit spectra for WASP-76 b transmission spectrum in high-resolution. A clear (no haze) upper atmosphere with a deep cloud-top (0.8 bar). Here the main opacities constitute H_2O, TiO and VO.
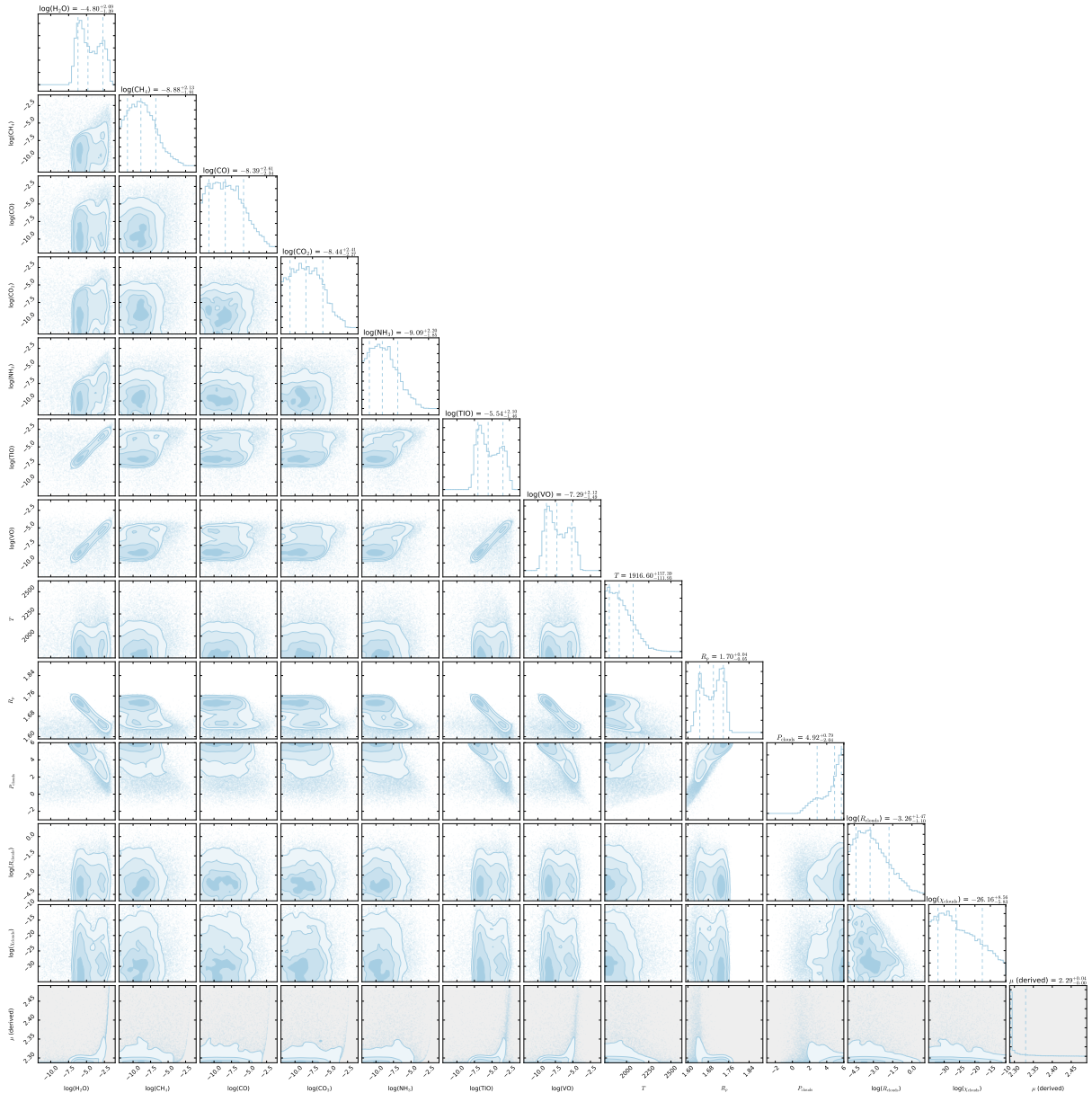
Figure 5. The posterior distribution of the Bayesian retrieval for WASP-76 b.

Table 1
Proposal information for the data used in our analysis.

Planet	Proposal ID	Proposal PI	Transits used	HST orbits used
GJ 436 b	11622	Heather Knutson	4	12
GJ 3470 b	13665	Bjoern Benneke	2	6
HAT-P-1 b	12473	David Sing	1	4
HAT-P-3 b	14260	Drake Deming	2	8
HAT-P-11 b	12449	Drake Deming	1	3
HAT-P-12 b	14260	Drake Deming	2	8
HAT-P-17 b	12956	Catherine Huitson	1	4
HAT-P-18 b	14260	Drake Deming	2	8
HAT-P-26 b	14260	Drake Deming	2	8
HAT-P-32 b	14260	Drake Deming	1	4
HAT-P-38 b	14260	Drake Deming	2	8
HAT-P-41 b	14767	David Sing	1	4
HD 149026 b	14260	Drake Deming	1	4
HD 189733 b	12881	Peter McCullough	1	6
HD 209458 b	12181	Drake Deming	1	4
WASP-12 b	13467	Jacob Bean	3	12
WASP-29 b	14260	Drake Deming	1	4
WASP-31 b	12473	David Sing	1	4
WASP-39 b	14260	Drake Deming	2	8
WASP-43 b	13467	Jacob Bean	6	18
WASP-52 b	14260	Drake Deming	1	3
WASP-63 b	14642	Kevin Stevenson	1	7
WASP-67 b	14260	Drake Deming	1	3
WASP-69 b	14260	Drake Deming	1	3
WASP-74 b	14767	David Sing	1	3
WASP-76 b	14260	Drake Deming	1	4
WASP-80 b	14260	Drake Deming	1	3
WASP-101 b	14767	David Sing	1	4
WASP-121 b	14468	Thomas Evans	1	4
XO-1 b	12181	Drake Deming	1	4

Table 2
Parameters used in our analysis. The transit mid-time and depth are not reported as they are fitted in all cases as free parameters.

Planet	$[\mathrm{Fe/H}]_*$	T_*	$\log(g_*)$	R_*	M_p	R_p	P	i	a/R_*	e	ω	Reference
		K	cgs	$R_\oplus$	M_Jup	R_Jup	days	deg			deg	
GJ 436 b	0.02	3416	4.843	0.455	0.08	0.366	2.64389754	86.858	14.54	0.1616	327.2	Lanotte et al. (2014)
GJ 3470 b	0.17	3652	4.78	0.48	0.043	0.346	3.3366487	88.88	13.94	-	-	Biddle et al. (2014)
HAT-P-1 b	0.13	5975	4.45	1.15	0.53	1.36	4.46529	85.9	10.247	-	-	Bakos et al. (2007)
HAT-P-3 b	0.27	5185	4.564	0.833	0.596	0.899	2.899703	87.24	10.59	-	-	Torres et al. (2008)
HAT-P-11 b	0.31	4780	4.59	0.75	0.081	0.422	4.8878162	88.55	15.58	0.198	355.2	Bakos et al. (2010)
HAT-P-12 b	-0.29	4650	4.61	0.701	0.211	0.959	3.2130598	89	11.77	-	-	Hartman et al. (2009)
HAT-P-17 b	0	5246	4.52	0.838	0.534	1.01	10.338523	89.2	22.63	0.346	201	Howard et al. (2012)
HAT-P-18 b	0.1	4870	4.57	0.717	0.196	0.947	5.507978	88.79	16.67	-	-	Esposito et al. (2014)
HAT-P-26 b	-0.04	5079	4.56	0.788	0.057	0.549	4.234515	88.6	13.44	-	-	Hartman et al. (2011a)
HAT-P-32 b	-0.04	6207	4.33	1.219	0.86	1.789	2.150008	88.9	6.05	-	-	Hartman et al. (2011b)
HAT-P-38 b	0.06	5330	4.45	0.923	0.267	0.825	4.640382	88.3	12.17	-	-	Sato et al. (2012)
HAT-P-41 b	0.21	6390	4.14	1.683	0.8	1.685	2.694047	87.7	5.44	-	-	Hartman et al. (2012)
HD 149026 b	0.36	6160	4.278	1.368	0.359	0.654	2.87598	90	7.17	-	-	Torres et al. (2008)
HD 189733 b	-0.03	5040	4.587	0.756	1.144	1.138	2.218573	85.58	8.81	-	-	Torres et al. (2008)
HD 209458 b	0	6065	4.361	1.155	0.685	1.359	3.524746	86.71	8.76	-	-	Torres et al. (2008)
WASP-12 b	0.33	6360	4.157	1.657	1.47	1.9	1.0914203	83.37	3.039	-	-	Collins et al. (2017)
WASP-29 b	0.11	4800	4.54	0.808	0.244	0.792	3.922727	88.8	12.415	-	-	Hellier et al. (2010)
WASP-31 b	-0.2	6302	4.308	1.252	0.478	1.549	3.4059096	84.41	8	-	-	Anderson et al. (2011)
WASP-39 b	-0.12	5400	4.503	0.895	0.28	1.27	4.055259	87.83	11.647	-	-	Faedi et al. (2011)
WASP-43 b	-0.05	4400	4.65	0.6	1.78	0.93	0.813475	82.6	5.124	-	-	Hellier et al. (2011)
WASP-52 b	0.03	5000	4.582	0.79	0.46	1.27	1.7497798	85.35	7.401	-	-	Hébrard et al. (2013)
WASP-63 b	0.08	5550	4.01	1.88	0.38	1.43	4.37809	87.8	6.773	-	-	Hellier et al. (2012)
WASP-67 b	-0.07	5200	4.5	0.87	0.42	1.4	4.61442	85.8	12.835	-	-	Hellier et al. (2012)
WASP-69 b	0.144	4715	4.535	0.813	0.26	1.057	3.8681382	86.71	11.953	-	-	Anderson et al. (2014)
WASP-74 b	0.39	5970	4.18	1.64	0.95	1.56	2.13775	79.81	4.861	-	-	Hellier et al. (2015)
WASP-76 b	0.23	6250	4.128	1.73	0.92	1.83	1.809886	88	4.012	-	-	West et al. (2016)
WASP-80 b	-0.13	4143	4.663	0.586	0.538	0.999	3.06785234	89.02	12.63	-	-	Triaud et al. (2015)
WASP-101 b	0.2	6380	4.345	1.29	0.5	1.41	3.585722	85	8.445	-	-	Hellier et al. (2014)
WASP-121 b	0.13	6460	4.242	1.458	1.183	1.865	1.2749255	87.6	3.754	-	-	Delrez et al. (2016)
XO-1 b	0.02	5750	4.509	0.934	0.918	1.206	3.941534	88.81	11.55	-	-	Torres et al. (2008)

Table 3
High-resolution spectra extracted for the planets in our sample. The values represent the transit depth $(R_{\mathrm{p}}/R_*)^2$ in ppm, for the 25 different wavelength channels.

GJ 436 b	GJ 3470 b	HAT-P-1 b	HAT-P-3 b	HAT-P-11 b	HAT-P-12 b	HAT-P-17 b	HAT-P-18 b	HAT-P-26 b	HAT-P-32 b	HAT-P-38 b	HAT-P-41 b	HD 149026 b	HD 189733 b	HD 209458 b
6995±50	6045±43	13783±90	11956±89	3532±57	18865±116	14721±82	18836±149	5145±75	23122±101	8726±125	10143±84	2574±26	24277±68	14589±34
6982±46	6014±44	13653±109	12193±82	3499±42	18830±111	14650±78	18793±103	5110±75	22953±128	8594±117	10385±95	2576±24	24315±71	14561±38
6954±44	5991±44	13583±98	12157±82	3567±45	18735±110	14542±90	18741±109	5021±84	22944±95	8666±116	10291±109	2581±27	24432±75	14578±38
6851±47	5993±45	13740±87	12166±79	3409±41	18752±103	14730±113	18647±116	5000±84	23024±114	8669±116	10336±87	2548±29	24303±86	14525±45
6959±41	6061±40	13685±108	12216±79	3544±34	18688±106	14648±79	18548±108	4921±77	23121±102	8644±77	10268±98	2548±29	24308±79	14523±38
7021±42	5972±40	13746±95	12190±72	3438±37	18634±122	14618±93	18410±111	5052±73	23092±105	8675±106	10340±99	2608±23	24235±88	14608±32
6989±43	5958±46	13539±98	12086±72	3401±42	18893±124	14712±76	18586±98	4919±84	22857±112	8705±86	10271±92	2589±23	24113±77	14515±32
6931±42	6050±46	13552±96	11998±84	3393±48	18842±132	14731±89	18608±125	5060±72	22868±99	8566±93	10228±107	2569±23	24173±65	14502±36
6957±40	5966±35	13596±89	12103±83	3475±49	18693±105	14876±77	18667±109	5034±63	23073±123	8661±103	10432±106	2632±27	24183±65	14562±38
7031±40	6040±41	13544±89	12208±85	3498±31	18711±101	14675±77	18803±99	5089±66	22914±118	8635±111	10256±83	2578±25	24328±77	14544±37
6974±39	6043±39	13738±87	12219±84	3490±31	18836±103	14756±81	18759±105	5103±70	23070±102	8532±114	10246±102	2579±22	24295±69	14498±41
6927±43	6095±37	13809±80	12208±79	3583±42	18661±113	14863±77	18720±100	5299±67	23297±141	8682±111	10448±78	2575±39	24315±67	14631±39
6976±41	6105±47	13577±116	12047±75	3538±37	19018±120	14828±87	18868±96	5368±67	23409±105	8744±111	10608±97	2602±27	24436±67	14681±33
6905±39	6026±45	13625±98	12055±96	3542±36	18797±89	14842±77	18781±97	5161±76	23314±89	8735±100	10375±102	2588±27	24414±62	14686±38
6944±42	6065±38	13879±93	12147±74	3538±40	18855±94	14602±79	18784±107	5365±64	23210±104	8869±129	10479±91	2579±22	24366±73	14744±35
7062±42	6071±41	14037±111	12111±85	3611±31	18970±95	14712±68	18862±97	5317±68	23429±99	8873±96	10553±84	2583±22	24441±85	14619±36
6915±41	6035±35	13885±106	12251±80	3613±42	18936±90	14631±86	18752±99	5282±61	23460±111	8790±133	10524±97	2634±25	24413±71	14630±45
6916±38	6037±40	13792±91	12173±88	3597±42	18652±88	14649±76	18813±83	5121±76	23137±121	8676±86	10515±109	2611±31	24311±70	14556±45
6924±39	6081±32	13972±96	12193±78	3552±39	18927±113	14617±83	18601±114	5283±67	23146±140	8875±114	10575±93	2638±24	24346±65	14620±37
6950±41	5999±34	13710±95	12139±81	3508±46	18642±114	14539±79	18547±112	5157±79	23105±202	8849±96	10542±115	2555±27	24259±69	14616±28
6958±37	6029±34	13713±117	12151±79	3490±47	18605±97	14621±78	18641±101	5025±79	23018±146	8839±97	10470±117	2602±26	24362±67	14602±39
6932±40	6065±39	13757±107	12186±93	3540±41	18614±110	14595±91	18693±97	4965±66	23133±114	8646±111	10437±102	2604±29	24118±59	14572±32
6913±39	6049±40	13708±114	12136±77	3416±47	18602±90	14537±114	18585±80	4914±74	23131±125	8529±106	10330±94	2588±27	24208±70	14579±34
6930±39	6031±36	13622±96	12182±76	3532±38	18768±90	14543±84	18492±124	4867±73	22792±113	8746±105	10242±121	2574±24	24213±70	14508±45
6947±37	6013±34	13431±98	12004±72	3534±40	18685±105	14655±84	18502±109	4861±73	22743±122	8580±91	10291±116	2520±26	24150±75	14588±42

WASP-12 b	WASP-29 b	WASP-31 b	WASP-39 b	WASP-43 b	WASP-52 b	WASP-63 b	WASP-67 b	WASP-69 b	WASP-74 b	WASP-76 b	WASP-80 b	WASP-101 b	WASP-121 b	XO-1 b
13904±60	9664±88	15698±197	21045±88	25423±61	27193±141	6195±64	26641±319	16552±55	9171±81	10917±52	29199±69	11830±110	14471±102	17317±121
13765±63	9702±89	15639±191	21133±86	25504±61	27075±140	6178±87	26355±352	16603±52	9072±94	10915±57	29230±77	11786±85	14684±72	17288±94
13817±63	9713±68	16001±184	21308±82	25390±52	27114±100	6132±60	27256±345	16558±40	9154±75	10880±47	29266±73	11817±107	14728±69	17519±92
13971±64	9600±67	15871±170	21126±82	25400±52	26831±133	6099±59	26581±283	16481±36	9108±68	10874±41	29300±67	11782±66	14708±83	17526±102
13912±63	9572±83	15945±140	20887±105	25332±58	26951±167	6135±60	26570±395	16451±56	9174±93	10834±46	29277±67	11943±77	14610±71	17366±104
13861±58	9642±73	15780±184	20927±101	25342±51	27138±161	6175±61	26125±237	16525±52	9142±68	10914±48	29237±58	11863±70	14626±77	17241±111
13848±58	9579±69	15741±139	20855±113	25402±53	26864±132	6078±53	26889±287	16508±41	9259±68	10842±39	29395±48	11961±74	14596±75	17363±98
13942±60	9673±73	16092±195	20894±94	25392±54	26896±113	6175±65	27003±326	16567±51	9241±78	10811±49	29294±54	11816±77	14567±75	17190±122
13855±61	9583±70	15632±206	21095±86	25351±54	26825±129	6215±57	26769±278	16523±38	9132±75	10756±54	29309±63	11838±80	14487±71	17278±102
13867±66	9597±81	15841±200	20947±85	25384±48	26926±124	6119±48	26280±338	16483±42	9126±68	10647±51	29244±57	11866±75	14511±92	17045±93
13918±58	9628±68	15543±206	20964±114	25367±47	27060±168	6257±52	26499±320	16505±40	9116±57	10715±35	29291±69	11920±58	14503±83	17203±145
14155±57	9527±62	15807±182	21148±69	25510±49	27349±147	6298±58	26527±348	16564±51	9202±69	10863±49	29375±51	11882±77	14789±72	17404±132
14143±59	9570±76	16113±140	21273±95	25480±51	27561±149	6246±54	27195±305	16609±54	9289±55	10913±41	29440±65	11825±86	14907±73	17593±134
13982±63	9639±64	15983±217	21317±92	25502±49	27685±130	6246±55	26935±311	16624±41	9278±70	10892±43	29440±51	11887±84	14791±88	17391±105
14073±55	9565±55	16064±163	21377±98	25431±52	27449±124	6257±62	26999±293	16606±45	9210±65	10809±41	-	11899±76	14835±88	17300±124
14090±59	9551±77	15936±162	21514±80	25439±45	27409±122	6206±52	27075±354	16608±47	9265±78	10887±36	29374±65	11797±74	14765±80	17493±104
14096±64	9560±73	15874±186	21447±112	25335±45	27157±157	6159±49	26643±370	16530±44	9206±75	10842±43	29322±53	11782±60	14749±74	17363±111
14119±59	9565±64	16070±139	21111±90	25363±49	27174±178	6212±56	26281±298	16548±40	9079±58	10832±38	29284±54	11865±57	14770±68	17472±106
14120±57	9551±72	16252±143	21486±98	25351±51	27113±154	6101±52	26573±285	16558±46	9159±80	10806±46	29276±49	11895±85	14607±87	17394±118
13952±60	9397±80	15780±179	21200±103	25388±58	26991±137	6187±62	26483±285	16542±53	9158±69	10846±39	29249±65	11728±74	14736±67	17469±110
14068±61	9638±86	15783±186	21081±85	25399±45	27068±165	6255±49	26552±264	16520±50	9090±75	10752±53	29288±51	11642±81	14672±86	17319±107
14028±63	9563±57	15671±188	20955±82	25339±48	26754±162	6173±59	26788±288	16436±41	9111±59	10714±56	29232±46	11621±86	14611±93	17231±113
13916±68	9487±67	15622±125	20906±96	25334±47	26781±168	6213±68	26381±303	16391±47	9037±74	10565±45	29270±61	11694±89	14542±69	17205±99
13886±66	9564±72	15950±220	20906±87	25271±51	26766±125	6126±67	26923±257	16384±52	9187±76	10612±44	29279±54	11707±81	14489±103	17272±104
13769±60	9514±72	15898±128	20656±116	25297±50	26962±155	6053±70	26373±250	16384±42	9031±67	10550±45	29326±56	11694±97	14283±93	17173±109

*Wavelength channels in μm: 1.1153–1.1372, 1.1372–1.1583, 1.1583–1.1789, 1.1789–1.1987, 1.1987–1.2180, 1.2180–1.2370, 1.2370–1.2559, 1.2559–1.2751, 1.2751–1.2944, 1.2944–1.3132, 1.3132–1.3320, 1.3320–1.3509, 1.3509–1.3701, 1.3701–1.3900, 1.3900–1.4100, 1.4100–1.4303, 1.4303–1.4509, 1.4509–1.4721, 1.4721–1.4941, 1.4941–1.5165, 1.5165–1.5395, 1.5395–1.5636, 1.5636–1.5889, 1.5889–1.6153, 1.6153–1.6436

Table 4
Observationally-corrected S/N, ADI, and main retrieval results for the planets analyzed.

Planet	o.c. S/N	ADI	R_{p}	T_{p}	$\log(P_{\mathrm{cloup-top}})$	$\log(\mathrm{H_2O})$
			R_{Jup}	K	P	
GJ 436 b	8.48	0.00	0.35 ± 0.01	613 ± 63	0.41 ± 1.75	-7.49 ± 2.54
GJ 3470 b	13.36	0.57	0.35 ± 0.01	660 ± 69	3.11 ± 1.21	-5.94 ± 2.13
HAT-P-1 b	9.05	6.72	1.27 ± 0.02	1319 ± 143	2.53 ± 1.11	-3.52 ± 1.23
HAT-P-3 b	4.58	0.11	0.87 ± 0.02	1123 ± 119	0.91 ± 2.07	-7.28 ± 2.64
HAT-P-11 b	6.28	9.35	0.42 ± 0.01	860 ± 89	3.36 ± 1.07	-3.39 ± 1.36
HAT-P-12 b	14.23	2.11	0.89 ± 0.02	911 ± 93	2.14 ± 1.13	-4.28 ± 1.61
HAT-P-17 b	4.89	0.56	0.97 ± 0.01	763 ± 80	0.61 ± 1.90	-6.88 ± 2.71
HAT-P-18 b	12.45	5.00	0.91 ± 0.02	795 ± 82	2.29 ± 1.08	-3.59 ± 1.20
HAT-P-26 b	11.52	41.79	0.53 ± 0.01	900 ± 94	4.75 ± 0.77	-5.26 ± 1.04
HAT-P-32 b	13.03	20.36	1.74 ± 0.03	1581 ± 127	2.33 ± 1.12	-3.59 ± 1.13
HAT-P-38 b	4.62	1.89	0.82 ± 0.01	1034 ± 115	3.12 ± 1.39	-3.88 ± 1.77
HAT-P-41 b	7.72	11.11	1.59 ± 0.03	1904 ± 200	2.22 ± 1.14	-3.29 ± 1.17
HD 149026 b	4.92	0.00	0.64 ± 0.01	1588 ± 167	0.05 ± 1.54	-6.74 ± 2.80
HD 189733 b	7.09	10.67	1.15 ± 0.01	1092 ± 108	3.37 ± 1.21	-3.69 ± 1.31
HD 209458 b	19.43	16.97	1.32 ± 0.01	1331 ± 121	1.86 ± 0.92	-3.36 ± 0.92
WASP-12 b	13.36	28.27	1.85 ± 0.03	2251 ± 154	2.65 ± 1.47	-3.84 ± 1.49
WASP-29 b	7.69	1.41	0.73 ± 0.01	895 ± 83	2.42 ± 2.14	-7.58 ± 2.39
WASP-31 b	7.83	1.42	1.44 ± 0.03	1472 ± 148	1.82 ± 1.05	-5.86 ± 2.61
WASP-39 b	20.42	36.70	1.19 ± 0.02	1082 ± 115	2.53 ± 0.94	-3.70 ± 1.01
WASP-43 b	6.29	2.42	0.94 ± 0.01	1321 ± 142	2.60 ± 1.96	-4.47 ± 2.05
WASP-52 b	12.13	26.59	1.24 ± 0.03	1141 ± 90	3.42 ± 1.42	-4.39 ± 1.51
WASP-63 b	10.32	0.68	1.35 ± 0.02	1401 ± 142	2.20 ± 0.96	-6.46 ± 2.42
WASP-67 b	5.38	0.14	1.32 ± 0.03	977 ± 105	1.15 ± 1.74	-6.17 ± 2.76
WASP-69 b	26.27	12.84	0.98 ± 0.02	944 ± 100	2.65 ± 1.11	-4.24 ± 1.12
WASP-74 b	7.43	0.12	1.46 ± 0.03	1832 ± 191	0.70 ± 1.58	-5.49 ± 2.68
WASP-76 b	20.06	37.26	1.69 ± 0.04	1890 ± 115	4.50 ± 1.30	-4.33 ± 1.76
WASP-80 b	14.24	2.87	0.97 ± 0.02	814 ± 87	1.48 ± 1.97	-6.16 ± 2.51
WASP-101 b	12.45	0.37	1.28 ± 0.02	1423 ± 136	1.05 ± 1.12	-7.31 ± 2.56
WASP-121 b	14.61	13.50	1.68 ± 0.03	1988 ± 91	4.32 ± 1.32	-4.04 ± 1.51
XO-1 b	4.51	3.75	1.20 ± 0.01	1096 ± 108	3.45 ± 1.35	-2.59 ± 1.57